INTERNATIONAL JOURNAL FOR NUMERICAL METHODS IN FLUIDS
Int. J. Numer. Meth. Fluids 2009; **59**:853–872
Published online 9 July 2008 in Wiley InterScience (www.interscience.wiley.com). DOI: 10.1002/fld.1843

Implicit–explicit finite-difference lattice Boltzmann method with viscid compressible model for gas oscillating patterns in a resonator

Yong Wang, Yaling He*,†, Jing Huang and Qing Li

State Key Laboratory of Multiphase Flow in Power Engineering, School of Energy & Power Engineering, Xi'an Jiaotong University, Xi'an, Shaanxi 710049, China

SUMMARY

Difficulties for the conventional computational fluid dynamics and the standard lattice Boltzmann method (LBM) to study the gas oscillating patterns in a resonator have been discussed. In light of the recent progresses in the LBM world, we are now able to deal with the compressibility and non-linear shock wave effects in the resonator. A lattice Boltzmann model for viscid compressible flows is introduced firstly. Then, the Boltzmann equation with the Bhatnagar–Gross–Krook approximation is solved by the finite-difference method with a third-order implicit–explicit (IMEX) Runge–Kutta scheme for time discretization, and a fifth-order weighted essentially non-oscillatory (WENO) scheme for space discretization. Numerical results obtained in this study agree quantitatively with both experimental data available and those using conventional numerical methods. Moreover, with the IMEX finite-difference LBM (FDLBM), the computational convergence rate can be significantly improved compared with the previous FDLBM and standard LBM. This study can also be applied for simulating some more complex phenomena in a thermoacoustics engine.

Received 5 December 2007; Revised 16 April 2008; Accepted 16 April 2008

KEY WORDS: lattice Boltzmann method; implicit–explicit; finite difference; compressible flow; gas oscillating

1. INTRODUCTION

The thermoacoustics can be simplistically defined as the physics of the interaction of thermal and acoustic fields [1]. In recent years, the thermoacoustics has been attracting more and more attentions as a major technology in the development of more efficient energy conversion/generation systems. However, the non-linear acoustic effects, the coupling between acoustic and thermal effects, the

*Correspondence to: Yaling He, State Key Laboratory of Multiphase Flow in Power Engineering, School of Energy & Power Engineering, Xi'an Jiaotong University, Xi'an, Shaanxi 710049, China.
†E-mail: yalinghe@mail.xjtu.edu.cn

Contract/grant sponsor: National Natural Science Foundation of China; contract/grant numbers: 50425620, 50736005

space and time multi-scale effects and the flows with porous medium in the thermoacoustics engines make it very complicated in theory. At the same time, it is also difficult to simulate performance of the thermoacoustics engines even for modern computer with the conventional computational fluid dynamics.

Taking the resonator for example, which is one of the most fundamental and important components in the thermoacoustics engines, considering a resonator driven by an oscillating plane piston at one end in the neighborhood of the fundamental resonant frequency of the gas column, periodic shock waves can be found traveling back and forth along the resonator with a frequency equal to that of the oscillating piston and velocity close to that of sound [2, 3]. As a result of the shock waves and oscillating flows, the heat and mass transport in a resonator can be enhanced dramatically compared with those beyond the resonant band. The understanding of gas oscillations in a resonator is of both fundamental and practical interest, and information about theoretical and experimental studies can be found in Ilgamov *et al.*'s review [4] and the references therein. However, there are a few published numerical simulations about this problem. This is because the appearance of the non-linear shock waves in resonant oscillations and the small *Ma* number of the gas flow require a high-resolution numerical scheme and a large computing resource. Moreover, most of these conventional simulations are restricted to solve just one-dimensional non-linear wave equations [5–8]. Recently, enumerable progresses with two-dimensional simulations are carried out. Alexeev and Gutfinger developed a two-dimensional numerical model for turbulent gas oscillations and studied the turbulence and acoustic streaming in a resonator with $l/L \geqslant 0.00597$ [3]. Here l and L are the oscillatory amplitude of the oscillating plane piston and the length of the resonator, respectively. Tang and Cheng solved the two-dimensional laminar gas flow in a cylindrical resonator with $l/L = 0.00186$ by a new finite-volume method with a second-order kinetic flux-vector splitting scheme for convective terms and a third-order Runge–Kutta method for the time evolution [9]. However, no quantitative comparison with previous results from experiment or numerical simulation was performed in their study.

The lattice Boltzmann method (LBM) is an alternative and promising numerical approach for studying the thermoacoustic problems. The LBM is different from the conventional numerical methods solving the macroscopic governing equations, e.g. Navier–Stokes (NS) equations for the conserved fields. Based on the kinetic theory, the LBM simulates fluid flows by tracking the evolution of particles taking on a few discrete velocities in discrete space at discrete time steps. It can easily model fluid flows with complicated boundary conditions. This means the LBM provides a method to obtain flow streams and heat transfer patterns for complicated systems from the microscopic and kinetic level [10–13]. On the basis of such viewpoint, we adopted the LBM to study phenomena systematically in a thermoacoustic engine. Our previous effort in this field can be found in Reference [14], in which we tried to simulate the two-dimensional gas oscillation in a resonator by the standard LBM. Here, 'standard' means the LBM is governed by the lattice Boltzmann equation with the Bhatnagar–Gross–Krook (BGK) approximations and evolved with streaming-collision procedure [15, 16]. Qualitative agreement between our numerical results and those using conventional numerical methods was obtained. However, due to the shortcomings of the standard LBM, such as its incompressible essentiality and lower convergence rate, quantitative agreement is limited even though the computations were carried out with high-performance computers.

Fortunately, in light of the recent progresses in the LBM world, we are now able to deal with the compressibility and non-linear shock wave effects in a resonator. We provide a brief review of these progresses as the following two sides.

DOI: 10.1002/fld

Various LBM models have been developed for compressible flow. The standard LBM is virtually regarded as a 'pseudo-compressibility method' [17]. Using the Chapman–Enskog expansion, the lattice Boltzmann equation in the standard LBM can yield the incompressible NS equations with additional terms that are of order *Ma* number squared. To breach this limit, several scholars developed LBM models that can recover the compressible Euler equations [18–20]. Alexander *et al.* [21] and Chen *et al.* [22] proposed LBM models for the compressible NS equations. However, the specific heat ratio γ in the previous models for the compressible NS equations cannot be chosen freely and is fixed at unphysical values. Subsequently, Kataoka and Tsutahara [23] developed a compressible NS model with a multi-speed lattice that overcomes the above defects. In their study, a variable about the rest energy, which comes from the internal motion of molecules, is introduced to satisfy the dissipation relation of energy and control the specific heat ratio. Numerical examples showed that their model could work well under the condition when *Ma* number is less than 1.0. Most recently, the rest energy is also used to adjust specific heat ratio in Reference [24].

On the other hand, some techniques to accelerate LBM are developed. Since the LBM can be regarded as a discrete velocity method for the Boltzmann equation with the BGK approximation, it is not surprising that there is a trend in the LBM world to use the finite-difference method [16, 17, 23, 25–34], the finite-volume method [24, 35–38] and the finite-element method [39] to improve the computational efficiency and accuracy. In the finite-difference LBM (FDLBM), the streaming-collision procedure in the standard LBM is replaced by the combination of finite-difference schemes for the convection term in the Boltzmann equation and step advancements in time. However, although fewer time steps are needed in the FDLBM than those in the standard LBM, because of some improved measures, such as using non-uniform meshes, the convergence rate in the FDLBM is still limited [34], especially in the case when the hyperbolic system described by the BGK Boltzmann equation is stiff (relaxation time much smaller than the time scale determined by the characteristic velocities of the system). To overcome such a flaw, we have proposed an implicit–explicit (IMEX) FDLBM in Reference [34]. Therein, we combined the IMEX Runge–Kutta scheme with the FDLBM. The relaxation term of the BGK Boltzmann equation is treated implicitly and the convection term explicitly. Thanks to the characteristic of the collision invariants in the LBM, no iteration is needed in practice. In other words, the implicitness is completely eliminated although the IMEX Runge–Kutta scheme is used. Numerical results of tests showed that the IMEX FDLBM can solve problems accurately and efficiently.

In this study, the LBM model derived by Kataoka and Tsutahara for the compressible NS equations is adopted to treat the compressible gas flows in a resonator. In order to overcome the shortcomings of the standard LBM mentioned above, the IMEX FDLBM is considered. Because of the high-order schemes and the compressible LBM model used in this study, quantitative agreement with both experimental data available and those using conventional numerical methods is obtained. More clear shock waves compared with those from the standard LBM are also observed. This is a part of an effort to study the thermoacoustic phenomena with the recent progresses of the LBM. This paper is organized as follows. In Section 2, details of the model for viscid compressible flows used in this study are introduced. In Section 3, a brief description of the IMEX FDLBM is given. In particular, the third-order IMEX Runge–Kutta scheme is adopted for time discretization, and the fifth-order WENO scheme is adopted for space discretization. In Section 4, the physical model of the resonator and the results obtained from the IMEX FDLBM simulations are presented. Finally, in Section 5, a brief conclusion of the present study is given.

DOI: 10.1002/fld

2. COMPRESSIBLE LBM MODEL

The present study uses the LBM model originally derived by Kataoka and Tsutahara for the compressible NS equations with a flexible specific heat ratio [23]. The evolution equation of the physical field is the BGK Boltzmann equation:

$$\frac{\partial f_i}{\partial t} + \mathbf{c}_i \cdot \nabla f_i = -\frac{f_i - f_i^{\mathrm{eq}}}{\tau} \tag{1}$$

where f_i ($i = 1, 2, \ldots, \mathscr{N}$; $\mathscr{N}$ is the total number of discrete particle velocities) is the particle density distribution function; t is the time; $\mathbf{c}_i$ is the discrete particle velocity along the ith direction; f_i^{eq} is the local equilibrium distribution function and τ is the relaxation time.

A two-dimensional version of this model with a multi-speed lattice (see Figure 1, $\mathscr{N} = 16$, $\alpha = 1, 2$) is given as

$$\frac{(c_{i1}, c_{i2})}{\sqrt{RT_0}} = \begin{cases} \mathrm{cyc}: (\pm 1, 0) & \text{for } 1 \leqslant i \leqslant 4 \\ \mathrm{cyc}: (\pm 6, 0) & \text{for } 5 \leqslant i \leqslant 8 \\ \sqrt{2}(\pm 1, \pm 1) & \text{for } 9 \leqslant i \leqslant 12 \\ \frac{3}{\sqrt{2}}(\pm 1, \pm 1) & \text{for } 13 \leqslant i \leqslant 16 \end{cases} \tag{2}$$

$$\frac{\eta_i}{\sqrt{RT_0}} = \begin{cases} \frac{5}{2} & \text{for } 1 \leqslant i \leqslant 4 \\ 0 & \text{for } 5 \leqslant i \leqslant 16 \end{cases} \tag{3}$$

where $c_{i\alpha}$ is the α component of $\mathbf{c}_i$; η_i is a variable introduced to control the specific heat ratio; cyc indicates the cyclic permutation; R is the specific gas constant and T_0 and $\sqrt{RT_0}$ are the

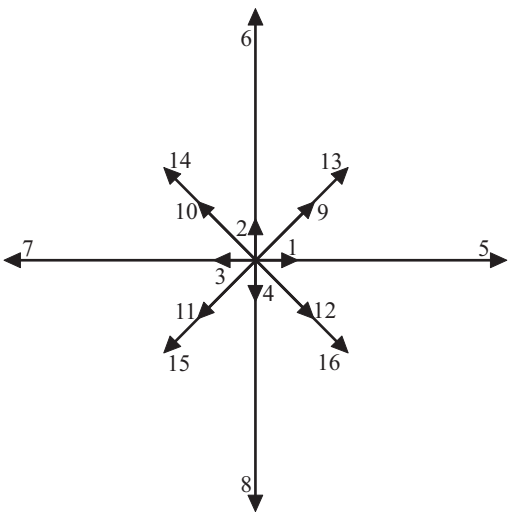

Figure 1. Multi-speed lattice of Kataoka and Tsutahara's model [23].

DOI: 10.1002/fld

characteristic temperature and velocity of the system, respectively. f_i^{eq} is defined as a function of macroscopic density ρ, velocity in α component u_α, temperature T as

$$f_i^{\mathrm{eq}} = \rho[a_{0i}+a_{1i}\bar{T}+a_{2i}\bar{T}^2+(a_{3i}+a_{4i}\bar{T})\bar{u}_\alpha^2+a_{5i}\bar{u}_\alpha^2\bar{u}_\beta^2+(b_{0i}+b_{1i}\bar{T}+b_{2i}\bar{u}_\alpha^2)\bar{u}_\beta^2\bar{c}_\beta^2$$
$$+(d_{0i}+d_{1i}\bar{T}+d_{2i}\bar{u}_\alpha^2)\bar{u}_\beta^2\bar{c}_\beta^2\bar{u}_\chi^2\bar{c}_\chi^2+e_i\bar{u}_\alpha^2\bar{u}_\alpha^2\bar{u}_\beta^2\bar{c}_\beta^2\bar{u}_\chi^2\bar{c}_\chi^2] \quad (i=1,\ldots,16;\ \alpha,\beta,\chi=1,2) \quad (4)$$

where the coefficients $a_{0i},\ldots,e_i$ are the given constants (see Table I); the variables with a bar in Equation (4), such as $\bar{T}$ and $\bar{u}_\alpha$, are the non-dimensional quantities with the characteristic ones mentioned above.

The macroscopic variables ρ, u_α and T are defined in terms of f_i as

$$\rho=\sum_{i=1}^{\mathscr{N}} f_i, \quad \rho u_\alpha=\sum_{i=1}^{\mathscr{N}} f_i c_{i\alpha}, \quad \rho(bRT+u_\alpha^2)=\sum_{i=1}^{\mathscr{N}} f_i(c_{i\alpha}^2+\eta_i^2) \quad (5)$$

where b is a given constant related to specific heat ratio γ with $\gamma=(b+2)/b$. We specially denote the collision invariants $\varphi\equiv(1,c_{i\alpha},c_{i\alpha}^2+\eta_i^2)$ in Equation (5). Moreover, transport coefficients are given by

$$\mu=\rho RT\tau, \quad \mu_{\mathrm{B}}=2(\tfrac{1}{3}-1/b)\rho RT\tau, \quad \lambda=(b+2)\rho R^2T\tau/2 \quad (6)$$

Table I. The coefficients $a_{0i},\ldots,e_i$ $(i=1,2,\ldots,16)$ in the local equilibrium distribution function f_i^{eq} given by Equation (4) [23].

i	1–4	5–8	9–12	13–16
a_{0i}	0	$\frac{1}{96}$	$\frac{81}{160}$	$\frac{-4}{15}$
a_{1i}	$\frac{b-2}{25}$	$\frac{-121b-408}{86400}$	$\frac{-229b+8}{3200}$	$\frac{89b+222}{2700}$
a_{2i}	0	$\frac{b+2}{1728}$	$\frac{b+2}{320}$	$\frac{-b-2}{270}$
a_{3i}	$\frac{-36}{115}$	$\frac{-799}{397440}$	$\frac{-117}{640}$	$\frac{-13}{135}$
a_{4i}	$\frac{b+4}{115}$	$\frac{19b+306}{397440}$	$\frac{9b+38}{640}$	$\frac{-2b-9}{270}$
a_{5i}	$\frac{1}{115}$	$\frac{19}{397440}$	$\frac{9}{640}$	$\frac{-1}{135}$
b_{0i}	0	0	$\frac{9}{40}$	$\frac{-2}{45}$
b_{1i}	$\frac{2(b-2)}{25}$	$\frac{-2b+29}{32400}$	$\frac{-14b+3}{400}$	$\frac{2(7b+11)}{2025}$
b_{2i}	0	$\frac{-1}{2592}$	$\frac{1}{80}$	$\frac{-7}{810}$
d_{0i}	$\frac{72}{115}$	$\frac{-29}{298080}$	$\frac{9}{160}$	$\frac{-2}{405}$
d_{1i}	$\frac{-2(b+4)}{115}$	$\frac{b+4}{74520}$	$\frac{-b-4}{160}$	$\frac{b+4}{810}$
d_{2i}	$\frac{-2}{115}$	$\frac{-2}{74520}$	$\frac{-1}{160}$	$\frac{1}{810}$
e_i	0	$\frac{1}{46656}$	$\frac{-3}{320}$	$\frac{8}{3645}$

DOI: 10.1002/fld

where μ, μ_B and λ are the dynamic viscosity, the bulk viscosity and the thermal conductivity, respectively. It should be noted that τ in this model is also a function of ρ and T, which is different from the standard LBM model with a constant relaxation time. Furthermore, in order to resolve the relaxation time in this model, Δt should be smaller than τ, such as $\Delta t = \tau/10$ for unsteady flows. If the condition that Knudsen number $\varepsilon = \tau(\rho_0, T_0)\sqrt{RT_0}/L_0 \ll 1$ (L_0 is the characteristic length of the system) is satisfied, the compressible NS equations can be derived from Equation (1) through the Chapman–Enskog expansion.

3. FORMULATION OF THE IMEX FDLBM

In the IMEX FDLBM, the so-called IMEX Runge–Kutta scheme, which solves the relaxation term (the right-hand side) of Equation (1) implicitly while other terms explicitly, is adopted for the time discretization [34]. The corresponding finite-difference schemes are adopted for space discretization. Owing to the characteristic of the collision invariants in the LBM, the implicitness can be completely eliminated, and thus no iteration is needed in practice. In this manner, problems (no matter stiff or not) can be integrated quickly with moderate Courant–Friedrichs–Lewy (CFL) number, which is defined as $C_{\mathrm{CFL}} = \Delta t \cdot \max\{c_{i1}, c_{i2}\}/\min\{\Delta x, \Delta y\}$ (Δt is the time spacing; Δx and Δy are the mesh spacing steps in x- and y-directions, respectively). Here we give a brief formulation of the IMEX FDLBM, and more details can be found in Reference [34].

3.1. Time discretization

To advance the distribution function f_i from time level n to $n+1$ in Equation (1) by the IMEX Runge–Kutta schemes, the following computations are conducted:

$$\sum_i^{\mathscr{N}} f_i^{(j)} \varphi = \sum_i^{\mathscr{N}} f_i^n \varphi - \Delta t \sum_{k=1}^{j-1} \tilde{m}_{jk} \left[\sum_i^{\mathscr{N}} (\mathbf{c}_i \cdot \nabla f_i^{(k)}) \varphi \right] \tag{7}$$

$$f_i^{(j)} = \frac{f_i^n - \Delta t \sum_{k=1}^{j-1} \tilde{m}_{jk} (\mathbf{c}_i \cdot \nabla f_i^{(k)}) + \Delta t \sum_{k=1}^{j-1} m_{jk} (f_i^{\mathrm{eq}(k)} - f_i^{(k)})/\tau^{(k)} + (\Delta t/\tau^{(j)}) m_{jj} f_i^{\mathrm{eq}(j)}}{1 + (\Delta t/\tau^{(j)}) m_{jj}} \tag{8}$$

and

$$f_i^{n+1} = f_i^n - \Delta t \sum_{j=1}^{r} \tilde{n}_j (\mathbf{c}_i \cdot \nabla f_i^{(j)}) + \Delta t \sum_{j=1}^{r} n_j \frac{f_i^{\mathrm{eq}(j)} - f_i^{(j)}}{\tau^{(j)}} \tag{9}$$

where $f_i^{()}$, $f_i^{\mathrm{eq}()}$, $\tau^{()}$ and j are the stage distribution function, the stage local equilibrium distribution function, the stage relaxation time and the stage number, respectively. The two $r \times r$ matrices $\tilde{M} = (\tilde{m}_{jk})$ ($\tilde{m}_{jk} = 0$ for $k \geqslant j$) and $M = (m_{jk})$ ($m_{jk} = 0$ for $k > j$) and the two vectors $\tilde{n} = (\tilde{n}_1, \ldots, \tilde{n}_r)^{\mathrm{T}}$ and $n = (n_1, \ldots, n_r)^{\mathrm{T}}$ characterize the IMEX Runge–Kutta schemes.

In summary, the updating rule of the variables is given as (i) with Equations (5) and (7), the jth stage macroscopic variables, such as $\rho^{(j)}$, $u_\alpha^{(j)}$ and $T^{(j)}$, can be calculated from $f_i^{()}$ of the previous stages; (ii) the corresponding $f_i^{\mathrm{eq}(j)}$ and $\tau^{(j)}$ of the current stage are updated with Equations (4) and (6); (iii) with Equation (8), $f_i^{(j)}$ of the current stage is calculated and (iv) after all the stages are carried out, we advance the distribution function f_i^n to the next level f_i^{n+1} with Equation (9).

DOI: 10.1002/fld

Table II. Tableau for the third-order IMEX Runge–Kutta scheme with four stages.

0	0	0	0	m_{11}	0	0	0
0	0	0	0	$-m_{11}$	m_{11}	0	0
0	1	0	0	0	$1-m_{11}$	m_{11}	0
0	$\frac{1}{4}$	$\frac{1}{4}$	0	m_{41}	m_{42}	$\frac{1}{2}-m_{11}-m_{41}-m_{41}$	m_{11}
0	$\frac{1}{6}$	$\frac{1}{6}$	$\frac{2}{3}$	0	$\frac{1}{6}$	$\frac{1}{6}$	$\frac{2}{3}$

$m_{11}=0.24169426078821$, $m_{41}=0.06042356519705$, $m_{42}=0.12915286960590$.

Moreover, the IMEX Runge–Kutta schemes can also be represented by a double Butcher's tableau as follows:

	$\tilde{M}$
	$\tilde{n}$

	M
	n

The coefficients of a third-order IMEX Runge–Kutta scheme with four stages [34] used in this study are given in Table II.

3.2. Space discretization

In this study, the fifth-order WENO scheme [34, 40] is adopted for the space discretization. In consideration of the x-component of the convection term $\mathbf{c}_i \cdot \nabla f_i$ in Equations (1) and (7)–(9), we give details of this scheme as

$$\frac{\partial(c_{i1} f_i)}{\partial x} = \frac{1}{\Delta x}(\widehat{F}_{i,I+1/2,J} - \widehat{F}_{i,I-1/2,J}) \tag{10}$$

where $\widehat{F}_{i,I+1/2,J}$ is the numerical flux at the interface of $x_I + \Delta x/2$ (I and J are node indexes) and is defined as

$$\widehat{F}_{i,I+1/2,J} = w_1 \widehat{F}^1_{i,I+1/2,J} + w_2 \widehat{F}^2_{i,I+1/2,J} + w_3 \widehat{F}^3_{i,I+1/2,J} \tag{11}$$

Under the condition $c_{i1} \geqslant 0$, three third-order fluxes on three different stencils $\widehat{F}^q_{i,I+1/2,J}$ ($q=1,2,3$) are given by

$$\widehat{F}^1_{i,I+1/2,J} = \tfrac{1}{3}F_{i,I-2,J} - \tfrac{7}{6}F_{i,I-1,J} + \tfrac{11}{6}F_{i,I,J} \tag{12a}$$

$$\widehat{F}^2_{i,I+1/2,J} = -\tfrac{1}{6}F_{i,I-1,J} + \tfrac{5}{6}F_{i,I,J} + \tfrac{1}{3}F_{i,I+1,J} \tag{12b}$$

and

$$\widehat{F}^3_{i,I+1/2,J} = \tfrac{1}{3}F_{i,I,J} + \tfrac{5}{6}F_{i,I+1,J} - \tfrac{1}{6}F_{i,I+2,J} \tag{12c}$$

where $F_{i,I,J} = c_{i1} f_{i,I,J}$.

The weighting factors w_q in Equation (11) are given by

$$w_q = \frac{\tilde{w}_q}{\tilde{w}_1 + \tilde{w}_2 + \tilde{w}_3}, \quad \tilde{w}_q = \frac{\delta_q}{(10^{-6} + \sigma_q)^2} \tag{13}$$

DOI: 10.1002/fld

with $\delta_1=\frac{1}{10}$, $\delta_2=\frac{3}{5}$ and $\delta_3=\frac{3}{10}$. The small value 10^{-6} is added to the denominator to avoid being divided by zero. The coefficients σ_q in Equation (13) are the smoothness indicators and can be obtained by

$$\sigma_1=\tfrac{13}{12}(F_{i,I-2,J}-2F_{i,I-1,J}+F_{i,I,J})^2+\tfrac{1}{4}(F_{i,I-2,J}-4F_{i,I-1,J}+3F_{i,I,J})^2 \tag{14a}$$

$$\sigma_2=\tfrac{13}{12}(F_{i,I-1,J}-2F_{i,I,J}+F_{i,I+1,J})^2+\tfrac{1}{4}(F_{i,I-1,J}-F_{i,I+1,J})^2 \tag{14b}$$

and

$$\sigma_3=\tfrac{13}{12}(F_{i,I,J}-2F_{i,I+1,J}+F_{i,I+2,J})^2+\tfrac{1}{4}(3F_{i,I,J}-4F_{i,I+1,J}+F_{i,I+2,J})^2 \tag{14c}$$

Similarly, under the condition $c_{i1}<0$, a mirror image procedure (with respect to $I+\frac{1}{2}$) of the procedure from Equations (12) to (14) can be carried out. For two-dimensional problems, this scheme should be applied in both x- and y-directions.

4. NUMERICAL RESULTS AND DISCUSSION

Numerical simulations are carried out for the gas flow and heat transfer characteristics in a resonator using the IMEX FDLBM introduced in Section 3. The compressible model adopted is introduced in Section 2, and more details can be found in Reference [23]. In a resonator, as shown in Figure 2, the oscillating flow is generated by a plane piston at the left end ($x=0$) with the velocity $l\omega\sin(\omega t)$ and reflected by the other closed end ($x=L=1.7018\,\mathrm{m}$). Here ω is the circular frequency. The resonator is filled with air under normal conditions and set as $\rho_0=1.165\,\mathrm{kg/m^3}$, $T_0=303\,\mathrm{K}$, $\mu=1.86\times10^{-5}\,\mathrm{kg/(m\,s)}$, $R=287\,\mathrm{J/(kg\,K)}$ and $\gamma=1.4$. The sound speed is defined as $c_s=\sqrt{\gamma RT_0}$. The fundamental resonant frequency of the tube is $\Omega=\pi c_s/L$. The frequency range to be considered is in the neighborhood of Ω.

In simulations, the computational domain $L\times H$ is covered by a non-uniform mesh with $\Delta x/\Delta y=\frac{1}{2}$ of size $N_x\times N_y$. For convenience, in consideration of the periodicity of the stack in the thermoacoustic refrigerator, which is the next effort of our study, the periodic boundary condition is applied to the y-direction in this study as

$$f_{i,I,0}=f_{i,I,N_y-1} \quad \text{at } y=0 \tag{15a}$$

$$f_{i,I,N_y}=f_{i,I,1} \quad \text{at } y=H \tag{15b}$$

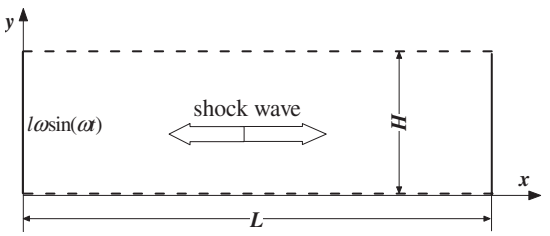

Figure 2. Schematic description of the resonator.

DOI: 10.1002/fld

This means the boundary layer effect is neglected in our simulation although a two-dimensional physical model is considered. Solid walls of the resonator are treated to be adiabatic, and the conditions imposed are as follows:

$$\left.\begin{aligned} u_{1,0,J} &= l\omega\sin(\omega t) \\ u_{2,0,J} &= 0 \\ T_{0,J} &= T_{1,J} \\ p_{0,J} &= (4p_{1,J} - p_{2,J})/3 \\ \rho_{0,J} &= p_{0,J}/RT_{0,J} \end{aligned}\right\} \quad \text{at } x = 0 \tag{16a}$$

$$\left.\begin{aligned} u_{1,N_x,J} &= 0 \\ u_{2,N_x,J} &= 0 \\ T_{N_x,J} &= T_{N_x-1,J} \\ p_{N_x,J} &= (4p_{N_x-1,J} - p_{N_x-2,J})/3 \\ \rho_{N_x,J} &= p_{N_x,J}/RT_{N_x,J} \end{aligned}\right\} \quad \text{at } x = L \tag{16b}$$

Macroscopic variables given in Equation (16) are used to update f_i^{eq} at the boundary nodes in the x-direction. Based on this, the non-equilibrium extrapolation method [41] is applied to obtain the unknown f_i at the boundary nodes:

$$f_{i,0,J} = f_{i,0,J}^{\mathrm{eq}} + (f_{i,1,J} - f_{i,1,J}^{\mathrm{eq}}) \quad \text{at } x = 0 \tag{17a}$$

$$f_{i,N_y,J} = f_{i,N_y,J}^{\mathrm{eq}} + (f_{i,N_y-1,J} - f_{i,N_y-1,J}^{\mathrm{eq}}) \quad \text{at } x = L \tag{17b}$$

In Figure 3, a mesh refinement study is considered firstly. The velocity and pressure near the closed end of the resonator ($x/L = 0.995$) at $\omega/\Omega = 1$ are obtained on different meshes with the mesh numbers $N_x \times N_y = 400 \times 40$, 600×60 and 800×80. The dimensionless time $tc_s/2L$ means the ordinal number of the oscillation period. We denote that the limit cycle state of the gas column has already been reached at $tc_s/2L = 15$ (see Figure 5(c)). As shown in Figure 3(a), there are minor phase differences between the velocity variations on different meshes. This is because for numerical stabilization, C_{CFL} is set to be 1.894 with different time spacing steps on different meshes. In other words, different meshes lead to different periods. It is also the reason why we used the dimensionless time $tc_s/2L$ instead of physical time or time step. Moreover, the maximum of the velocity with mesh $N_x \times N_y = 600 \times 60$ is close to that of $N_x \times N_y = 800 \times 80$, and both of them are larger than that of $N_x \times N_y = 400 \times 40$. In Figure 3(b), the phase differences of the pressure variations also exist, and the discrepancy between the amplitudes of the pressure is not significant. Thus, it may be concluded that $N_x \times N_y = 600 \times 60$ is competent for the simulations of this paper and is employed in the following computations.

Figure 4 gives a comparison of the pressure oscillation form, which is calculated at the closed end ($x/L = 1.0$) and $\omega/\Omega = 1$, with the results from Aganin *et al.*'s model A [7] and the experimental data of Saenger and Hudson [2]. For $l/L = 0.00161$, as shown in Figure 4(a), the difference between the maximum and minimum pressure over a period in Aganin *et al.*'s model A is 28.6% [7],

DOI: 10.1002/fld

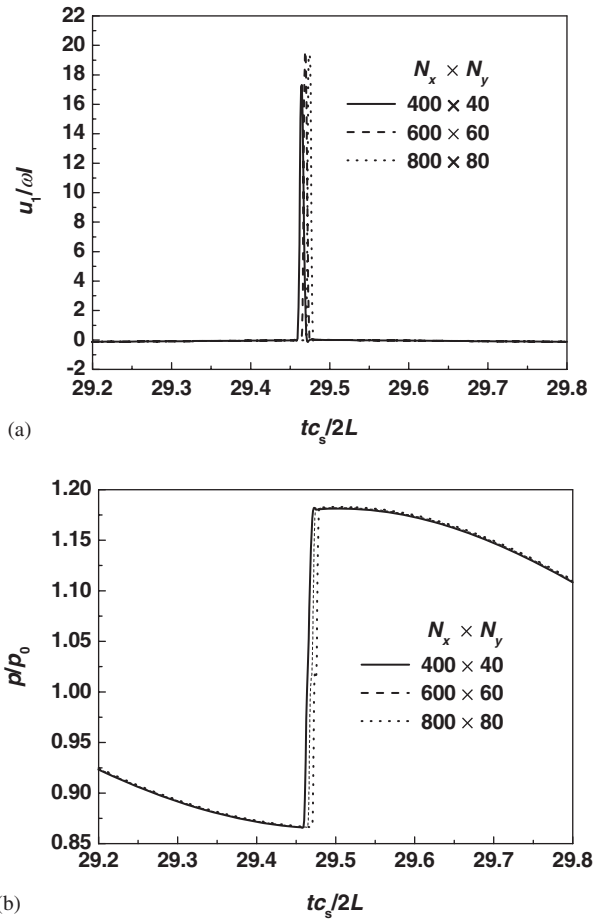

Figure 3. Mesh refinement study of the time-dependent (a) velocity and (b) pressure near the closed end of the resonator ($x/L=0.995$) with adiabatic walls at $\omega/\Omega=1$.

and 28.8% in our study. Good agreement between the numerical results with those using conventional numerical methods is obtained. For $l/L=0.00186$, the difference between the maximum and minimum pressure over a period in Saenger and Hudson's experiment is 216 mmHg/760 mmHg $\doteq$ 28.4% [2], and 31.1% in our study. Small discrepancy between the numerical results and experimental data is due to the boundary layer effect, which is not taken into account in our simulation. Nevertheless, the feasibility of the IMEX FDLBM and relevant code are validated. Moreover, periodic pulse-type jumps that indicate the propagation of the shock waves are captured clearly. In the following computations, l/L is set to be 0.00186 unless otherwise mentioned.

Figure 5 presents the pressure near the closed end of the resonator ($x/L=0.995$) for five frequencies in the neighborhood of Ω. It refers to the entire interval $0\leqslant tc_s/2L\leqslant 50$ and provides an idea of the overall processes. It can be observed that rapid increases in the oscillation amplitudes occur at all frequencies presented over some initial periods. Then for the frequencies close to Ω ($\omega/\Omega=0.97$, 1.0 and 1.03), the systems reach their corresponding limit cycle states and the

DOI: 10.1002/fld

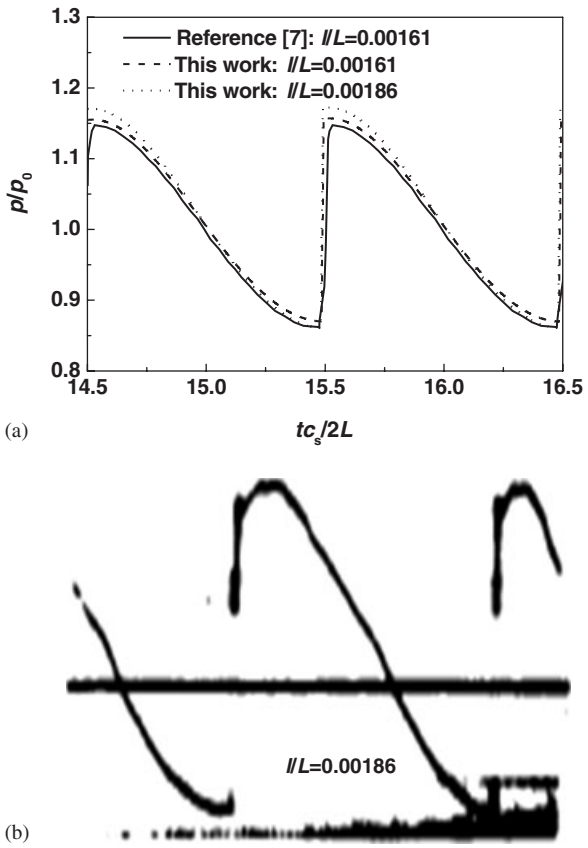

Figure 4. (a) Comparison of the numerical results in this study with Aganin *et al.*'s numerical results [7]. (b) The experimental results of Saenger and Hudson [2]. The pressure is calculated at the closed end ($x/L=1.0$). The values of l/L in References [7] and [2] are 0.00161 and 0.00186, respectively. Both parameters are considered in the validation of our code.

envelopes of the oscillating pressure are smooth. When the frequencies are further away from the resonant frequency ($\omega/\Omega=0.95$ and 1.05), the envelopes of the oscillating pressure are saw toothed, because of the beating produced by the frequency difference $\omega-\Omega$ [7]. The saw teeth at $\omega/\Omega=0.95$ point to the direction of the time, whereas at $\omega/\Omega=1.05$ the direction is reversed.

More details of the oscillation waveforms of the pressure for different frequencies are presented in Figure 6. Two intervals ($30\leqslant tc_s/2L\leqslant 32$ and $40\leqslant tc_s/2L\leqslant 42$) are considered for comparison. It can be seen from Figure 6 that the waveforms transform with the change in the frequencies. Periodical pulse-type jumps are observed in pressure at $\omega/\Omega=1.0$, which indicates the propagation of a shock wave. When the frequencies depart from the resonance ($\omega/\Omega=0.97$ and 1.03), the shock waves are also numerically captured. The pre-resonant oscillation form ($\omega/\Omega=0.97$) is distinctive in that it is adjacent to the maximum over a period after a pulse-type jump; however, the post-resonant oscillation form ($\omega/\Omega=1.03$) has a maximum immediately after the jump. When the frequencies are far away from the resonant frequency ($\omega/\Omega=0.95$ and 1.05), the waveforms are approximately sine waves with periodically slight jump. Moreover, the waveforms in two

DOI: 10.1002/fld

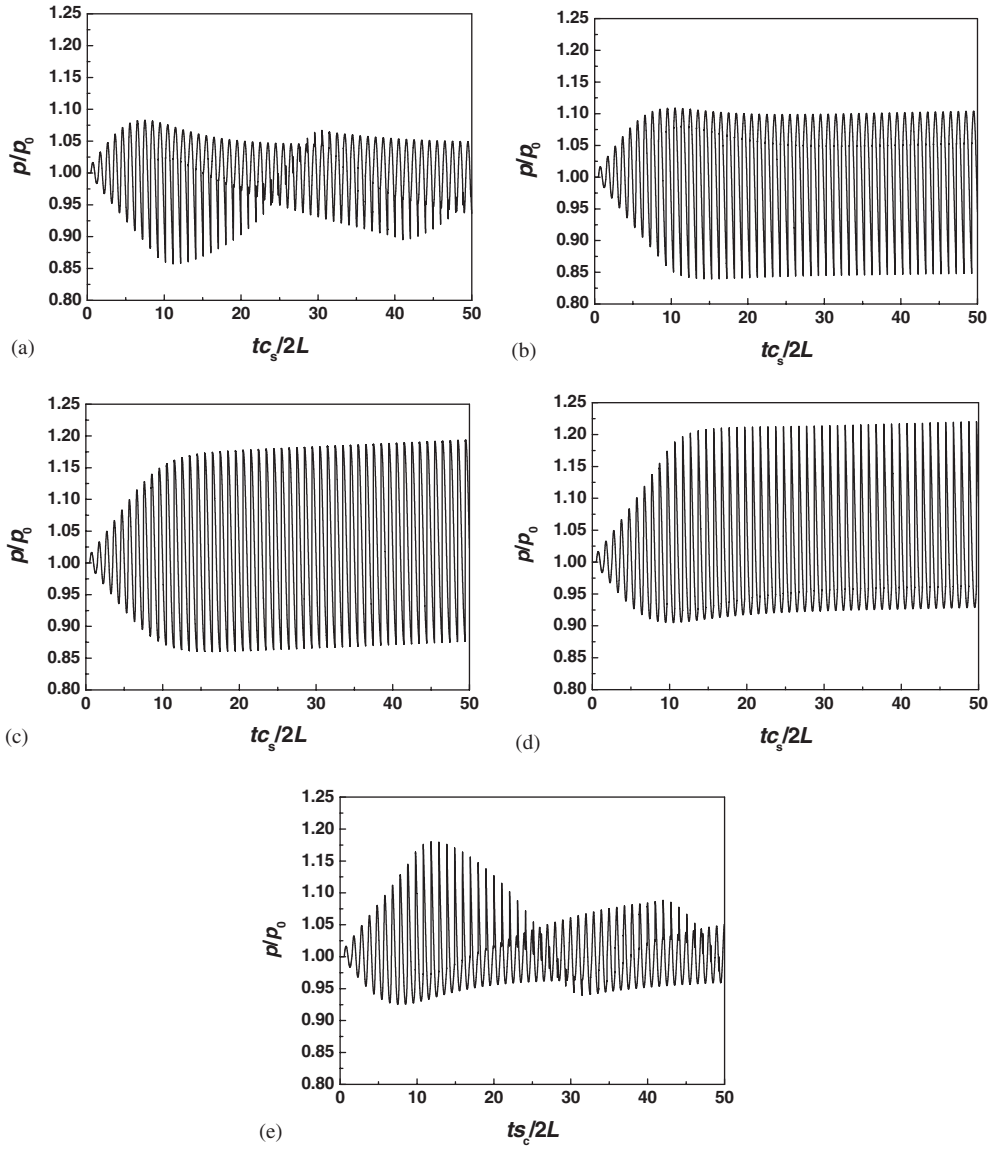

Figure 5. Time histories of the pressure near the closed end of the resonator ($x/L=0.995$) with adiabatic walls for five frequencies in the neighborhood of Ω: (a) $\omega/\Omega=0.95$; (b) $\omega/\Omega=0.97$; (c) $\omega/\Omega=1.0$; (d) $\omega/\Omega=1.03$; and (e) $\omega/\Omega=1.05$.

intervals are almost in phase with each other when the frequencies are close to Ω, whereas when the frequencies are far away from the resonant frequency ($\omega/\Omega=0.95$ and 1.05) the waveforms are not in phase.

Then, we focus on the gas oscillating patterns at the fundamental resonant frequency. Gas flow and heat transfer characteristics under the limit cycle condition are studied. Figure 7 presents

DOI: 10.1002/fld

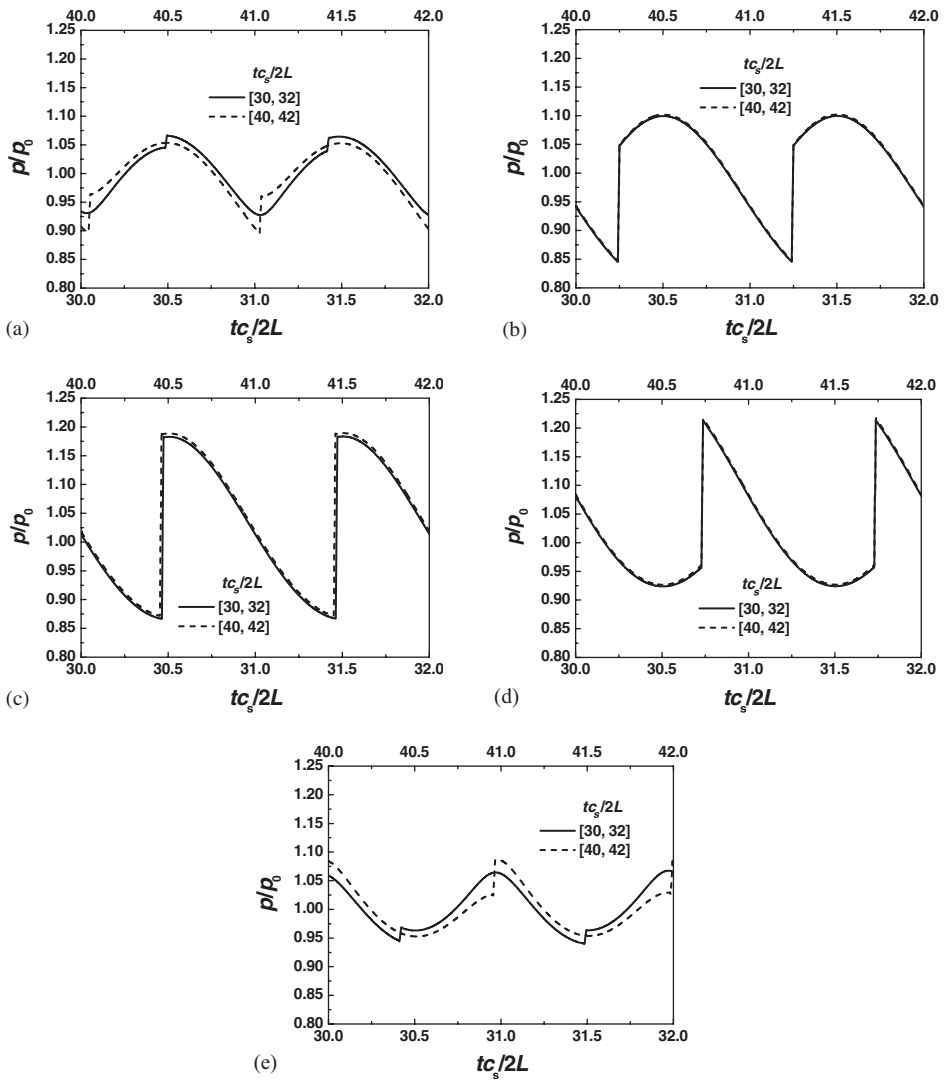

Figure 6. Pressure oscillation forms near the closed end of the resonator ($x/L=0.995$) in two intervals ($30\leqslant tc_s/2L\leqslant 32$ and $40\leqslant tc_s/2L\leqslant 42$) with adiabatic walls for five frequencies in the neighborhood of Ω: (a) $\omega/\Omega=0.95$; (b) $\omega/\Omega=0.97$; (c) $\omega/\Omega=1.0$; (d) $\omega/\Omega=1.03$; and (e) $\omega/\Omega=1.05$.

the temporal variations of the velocity, pressure and temperature at three locations ($x/L=0.005$, 0.5 and 0.995) along the x-direction of the resonator with adiabatic walls at $\omega/\Omega=1.0$. From Figure 7(a), it can be seen that the waveform of velocity at $x/L=0.005$ is almost sinusoidal with the piston movement, and a sudden pulse-type change occurs when the shock wave travels through this location. Waveforms of velocity at $x/L=0.5$ and 0.995 are also given. It can be observed that the phase difference between the velocity at $x/L=0.005$ and 0.5 is about 90°, and the phase difference between the velocity at $x/L=0.5$ and 0.995 is also 90°.

DOI: 10.1002/fld

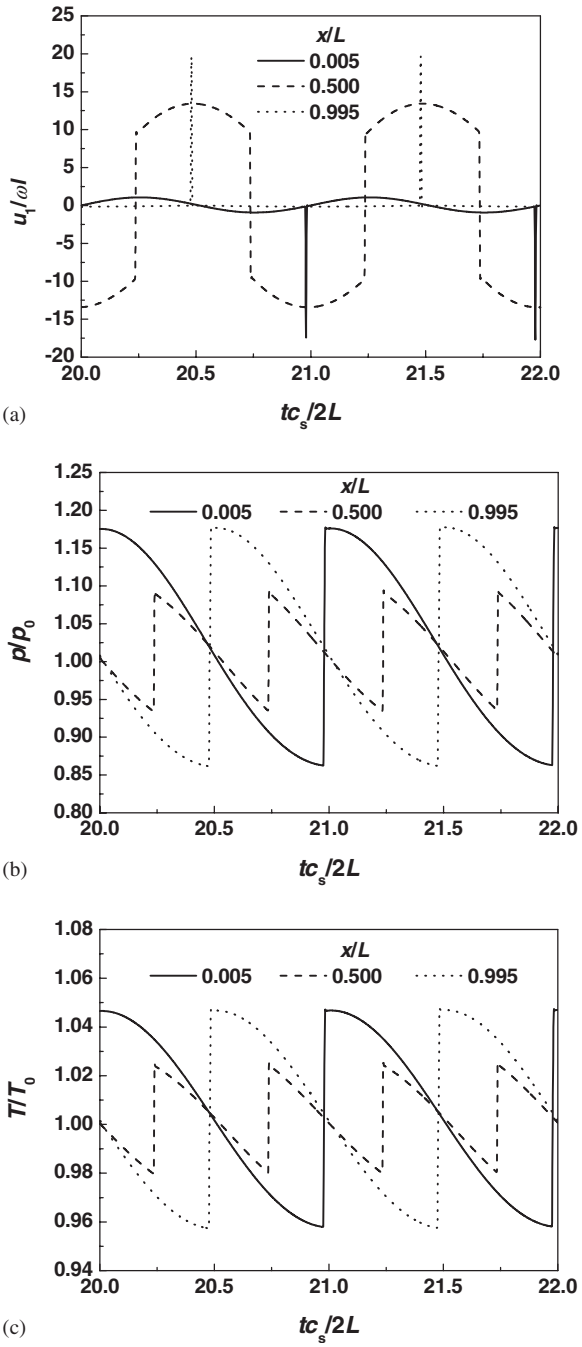

Figure 7. Temporal variations of the (a) velocity, (b) pressure and (c) temperature at three locations along the x-direction of the resonator with adiabatic walls at $\omega/\Omega = 1.0$.

DOI: 10.1002/fld

From Figure 7(b), it can be seen that the amplitude of the oscillating pressure at $x/L=0.5$ is smaller than that of the oscillating pressure at $x/L=0.005$ and 0.995. Moreover, the pressure increases sharply at the same time of the velocity's pulse-type change at the corresponding location. In comparison with Figures 7(a) and (b), the phase difference between the velocity and pressure at the same location is 90° (see the lines of $x/L=0.5$ at Figures 7(a) and (b) for a legible observation). It should be noted that because of the symmetry of geometry, two wave crests of the pressure in one oscillation period are observed in $x/L=0.5$. Corresponding temporal variations of the temperature are presented in Figure 7(c). It is shown that the characteristics of the temporal oscillating temperature are similar to those of the oscillating pressure. Furthermore, in comparison with Figures 7(b) and (c), the pressure and temperature are in phase with each other. In consideration of the relation between pressure, temperature and density, which is described as the state equation, we denote that the density and pressure are also in phase with each other. In addition, similar phenomena of the temporal velocity, pressure and temperature are presented in Figures 3–5 for adiabatic walls in Reference [9].

Figure 8 presents the fast Fourier transform of the pressure signal at the location of $x/L=0.995$ under the fundamental resonant frequency. P_a is the amplitude of the oscillating pressure. The existence of the non-linear acoustic effect can be observed clearly from Figure 8. Although the main component of the pressure signal is fundamental, the second and other higher harmonic ones are also obvious.

Figure 9 presents the distributions of the velocity and density along the x-direction of the resonator at different times of a period at $\omega/\Omega=1.0$. It is observed that shock wave travels back and forth along the x-direction of the resonator. Figure 9(a) indicates that the wave nodes of the oscillating velocity are fixed near the walls and the wave loops are unfixed along the resonator. Figure 9(b) refers to the half period $49.5<tc_s/2L<50$. It indicates that both the wave nodes and loops of the oscillating density (or pressure) are unfixed. Furthermore, we denote that during the other half period ($49<tc_s/2L<49.5$), the distributions of the density (or pressure) are mirror-symmetrical with respect to $x/L=0.5$.

Figure 10(a) shows the time dependence of the temperature at the middle point of the resonator ($x/L=0.50$) in two intervals ($19\leqslant tc_s/2L\leqslant 20$ and $49\leqslant tc_s/2L\leqslant 50$) with adiabatic walls at

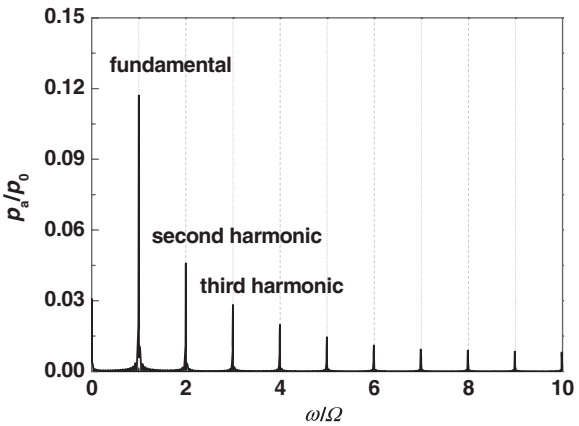

Figure 8. Fast Fourier transform of the pressure at the location of $x/L=0.995$ under the fundamental resonant frequency. P_a is the amplitude of the oscillating pressure.

DOI: 10.1002/fld

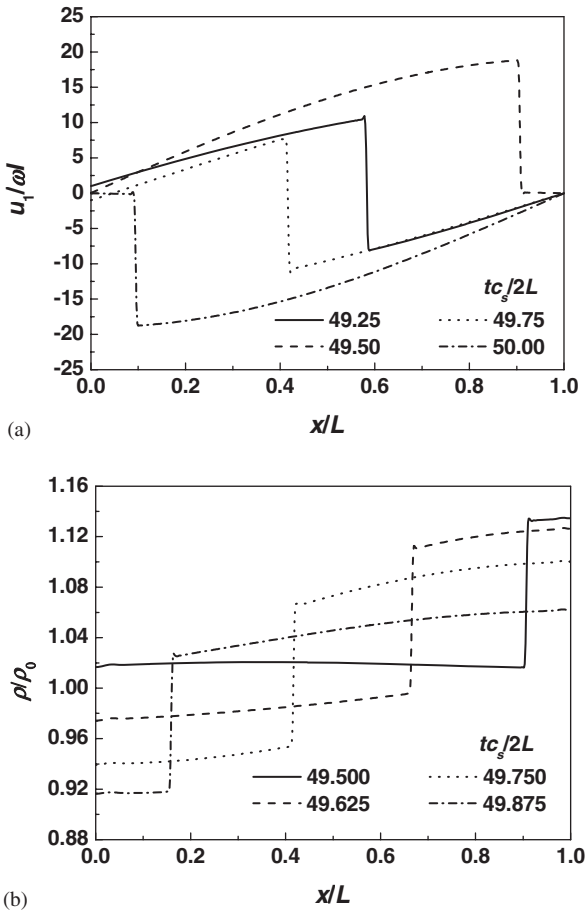

Figure 9. Development of the (a) velocity and (b) density profiles along the x-direction of the resonator with adiabatic walls at $\omega/\Omega = 1.0$.

$\omega/\Omega = 1.0$. It can be seen that the gas temperature increases with the time. A more detailed description about the time-dependent temperatures can be found in Figure 10(b), where the temperatures presented were averaged over one oscillation period and three locations along the x-direction of the resonator are considered. It is seen that, after some initial periods, the period averaging temperatures increase linearly with the increase in the time, because the state of the gas column is essentially periodically unsteady with adiabatic walls.

Finally, we denote that, in this study, the shock waves in the resonator are numerical captured more legibly than those in our previous study with standard LBM [14]. As the gas oscillation in the resonator is compressible essentially, an LBM model for viscid compressible NS flows can treat such a problem better than the incompressible model in the standard LBM. The high-order schemes for the space and time discretization in the IMEX FDLBM also lead to good performance in capturing the shock waves. Moreover, in consideration of $\mu = \rho R T \tau$ in Equation (6) and the macroscopic parameters given as above, τ is at the order of 10^{-10} s, and much smaller

DOI: 10.1002/fld

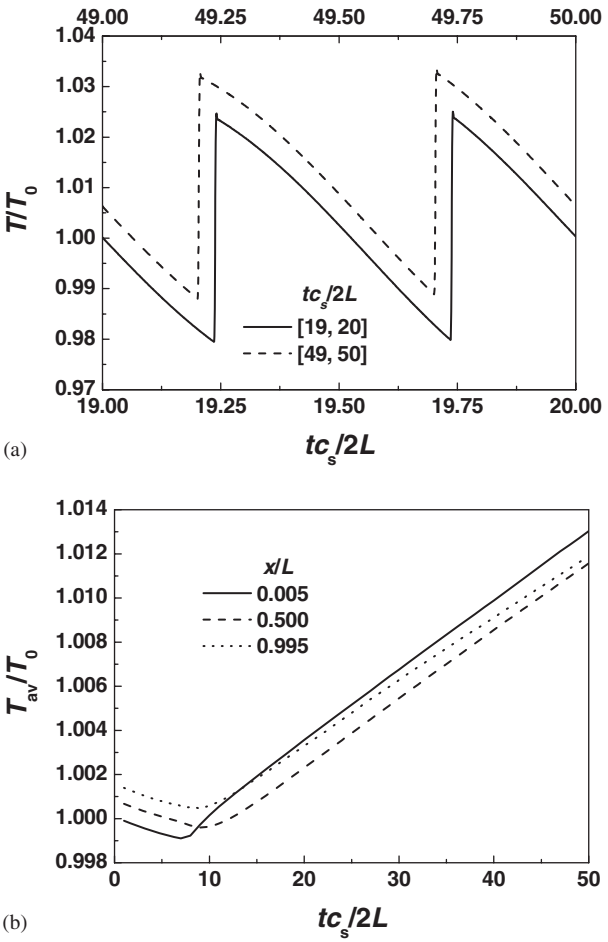

Figure 10. (a) Time dependence of the temperature at the middle point of the resonator ($x/L=0.50$) in two intervals ($19\leqslant tc_s/2L\leqslant 20$ and $49\leqslant tc_s/2L\leqslant 50$) and (b) period averaging temperatures at three locations along the x-direction of the resonator with adiabatic walls at $\omega/\Omega=1.0$.

than the period of the oscillating gas, which is about 0.01 s. For $N_x\times N_y=600\times 60$ used in our simulations, $\Delta t=\tau\times 10^5/3$ is set with $C_{\mathrm{CFL}}=1.894$ instead of $\Delta t=\tau/10$, which is needed for unsteady flow in the compressible NS model introduced in Section 2. As a result, with the IMEX FDLBM, the computational convergence rate of this stiff problem can be significantly improved, and the convergence rate is accelerated to 3.33×10^5 times in our simulations. This study leads to the feasibility to simulate fluid flow and heat transfer in a more complex thermoacoustic engine using the new progresses in the LBM field. In particular, numerical studying on the self-excited onset process of a thermoacoustic prime mover named thermoacoustic instability is underway in our group. The non-linear acoustic effect and space and time multi-scale effects in such a phenomenon make the simulation very difficult, and relevant results will be presented elsewhere.

DOI: 10.1002/fld

5. CONCLUSION

In this paper, the IMEX FDLBM is adopted to simulate the gas oscillating patterns in a resonator with adiabatic walls. Shock waves are numerically captured when the oscillating plane piston is at the resonant frequency or slightly off-resonant frequencies. Waveforms of the oscillating pressure at different frequencies are contrasted with each other. Specially, the gas flow and heat transfer characteristics at resonant frequency are numerical studied in detail. Temporal variations of the velocity, pressure and temperature at various locations of the resonator at resonant frequency are presented. Phase differences between the oscillating velocity and pressure is 90°, whereas the pressure, temperature and density are in phase with each other. The wave nodes of the oscillating velocity are fixed near the walls and the wave loops are unfixed along the resonator, whereas both the wave nodes and loops of the oscillating density (or pressure) are unfixed. Since the state of the gas column is essentially periodically unsteady with adiabatic walls, it is observed that period averaging temperatures increase linearly with the increase in the time after some initial periods.

Numerical results obtained in this study agree quantitatively well with experimental data available and those using conventional numerical methods. Moreover, with the IMEX FDLBM, the computational convergence rate can be significantly improved compared with the previous FDLBM and the standard LBM. This is a part of an effort to better understand the fundamentals of the thermoacoustic phenomena with the recent progresses of the LBM. It is proved that the LBM can be used in the thermoacoustic field and obtain satisfied quantitative results. The IMEX FDLBM used here is now being employed for ongoing study on simulating the non-linear thermoacoustic instabilities in a thermoacoustic prime mover.

ACKNOWLEDGEMENTS

The present study was supported by the National Natural Science Fund for Distinguished Young Scholars from the National Natural Science Foundation of China (No. 50425620), the Key Project of National Natural Science Foundation of China (No. 50736005).

REFERENCES

1. Gopinath A, Tait NL, Garrett SL. Thermoacoustic streaming in a resonant channel: the time averaged temperature distribution. *Journal of the Acoustical Society of America* 1998; **103**(3):1388–1405.
2. Saenger RA, Hudson GE. Periodic shock waves in resonating gas columns. *Journal of the Acoustical Society of America* 1960; **32**:961–971.
3. Alexeev A, Gutfinger C. Resonance gas oscillations in closed tubes: numerical study and experiments. *Physics of Fluids* 2003; **15**(11):3397–3408.
4. Ilgamov MA, Zaripov RG, Galiullin RG, Repin VB. Nonlinear oscillations of a gas in a tube. *Applied Mechanics Reviews* 1996; **49**(3):137–154.
5. Lee CP, Wang TG. Nonlinear resonance and viscous dissipation in an acoustic chamber. *Journal of the Acoustical Society of America* 1992; **92**:2195–2206.
6. Elvira-Segura L, Sarabia E. Numerical and experimental study of finite-amplitude standing waves in a tube at high sonic frequencies. *Journal of the Acoustical Society of America* 1998; **104**:708–714.
7. Aganin AA, Ilgamov MA, Smirnova ET. Development of longitudinal gas oscillations in a closed tube. *Journal of Sound and Vibration* 1996; **195**(3):359–374.
8. Christian V, Cleofe CP. Numerical model for nonlinear standing waves and weak shocks in thermoviscous fluids. *Journal of the Acoustical Society of America* 2001; **109**(6):2660–2667.
9. Tang HZ, Cheng P. Numerical simulations of resonant oscillation in a tube. *Numerical Heat Transfer*, *Part A* 2001; **40**:37–54.

DOI: 10.1002/fld

10. Buick JM, Greated CA, Campbell DM. Lattice BGK simulation of sound wave. *Europhysics Letters* 1998; **43**(3):235–240.
11. Haydock D, Yeomans JM. Lattice Boltzmann simulations of acoustic streaming. *Journal of Physics A*: *Mathematical and General* 2001; **34**:5201–5213.
12. Li XM, Leung RCK, So RMC. One-step aeroacoustics simulation using lattice Boltzmann method. *AIAA Journal* 2006; **44**(1):78–89.
13. Kang H, Tsutahara M. An application of the finite difference-based lattice Boltzmann model to simulating flow-induced noise. *International Journal for Numerical Methods in Fluids* 2007; **53**:629–650.
14. Wang Y, He YL, Li Q, Tang GH. Numerical simulations of gas resonant oscillations in a closed tube using lattice Boltzmann method. *International Journal of Heat and Mass Transfer* 2008; **51**:3082–3090.
15. Chen SY, Doolen GD. Lattice Boltzmann method for fluid flows. *Annual Review of Fluid Mechanics* 1998; **30**(1):329–364.
16. Cristea A, Gonnella G, Lamura A, Sofonea V. Finite-difference lattice Boltzmann model for liquid–vapor systems. *Mathematics and Computers in Simulation* 2006; **72**:113–116.
17. Reider MB, Sterling JD. Accuracy of discrete-velocity BGK models for the simulation of the incompressible Navier–Stokes equations. *Computers and Fluids* 1995; **24**(4):459–467.
18. Yan G, Chen Y, Hu S. Simple lattice Boltzmann model for simulating flows with shock wave. *Physical Review E* 1999; **59**(1):454–459.
19. Shi WP, Shyy W, Mei RW. Finite-difference-based lattice Boltzmann method for inviscid compressible flows. *Numerical Heat Transfer*, *Part B* 2001; **40**:1–21.
20. Kataoka T, Tsutahara M. Lattice Boltzmann method for the compressible Euler equations. *Physical Review E* 2004; **69**:056702.
21. Alexander FJ, Chen S, Sterling JD. Lattice Boltzmann thermohydrodynamics. *Physical Review E* 1993; **47**(4): 2249–2252.
22. Chen Y, Ohashi H, Akiyama M. Thermal lattice Bhatnagar–Gross–Krook model without nonlinear deviations in macrodynamic equations. *Physical Review E* 1994; **50**:2776–2783.
23. Kataoka T, Tsutahara M. Lattice Boltzmann model for the compressible Navier–Stokes equations with flexible specific-heat ratio. *Physical Review E* 2004; **69**:035701.
24. Qu K, Shu C, Chew YT. Alternative method to construct equilibrium distribution functions in lattice-Boltzmann method simulation of inviscid compressible flows at high Mach number. *Physical Review E* 2007; **75**:036706.
25. Cao N, Chen S, Jin S, Martinez D. Physical symmetry and lattice symmetry in the lattice Boltzmann method. *Physical Review E* 1997; **55**(1):21–24.
26. Mei R, Shyy W. On the finite difference-based lattice Boltzmann method in curvilinear coordinates. *Journal of Computational Physics* 1998; **143**:426–448.
27. Tolke J, Krafczyk M, Schulz M, Rank E. Implicit discretization and nonuniform refinement approaches for FD discretizations of LBGK models. *International Journal of Modern Physics C* 1998; **9**(8):1143–1157.
28. Guo Z, Zhao TS. Explicit finite-difference lattice Boltzmann method for curvilinear coordinates. *Physical Review E* 2003; **67**:066709.
29. Watari M, Tsutahara M. Two-dimensional thermal model of the finite-difference lattice Boltzmann method with high spatial isotropy. *Physical Review E* 2003; **67**:036306.
30. Kim I, Lindquist WB, Durham WB. Fracture flow simulation using a finite-difference lattice Boltzmann method. *Physical Review E* 2003; **67**:046708.
31. Sofonea V, Lamura A, Gonnella G, Cristea A. Finite-difference lattice Boltzmann model with flux limiters for liquid–vapor systems. *Physical Review E* 2004; **70**:046702.
32. Guo Z, Zhao TS. Finite-difference-based lattice Boltzmann model for dense binary mixtures. *Physical Review E* 2005; **71**:026701.
33. Xu A. Finite-difference lattice-Boltzmann methods for binary fluids. *Physical Review E* 2005; **71**:066706.
34. Wang Y, He YL, Zhao TS, Tang GH, Tao WQ. Implicit–explicit finite-difference lattice Boltzmann method for compressible flows. *International Journal of Modern Physics C* 2007; **18**(12):1961–1983.
35. Nannelli F, Succi S. The lattice Boltzmann equation in irregular lattices. *Journal of Statistical Physics* 1992; **68**:401–407.
36. Chen H. Volumetric formulation of the lattice Boltzmann method for fluid dynamics: basic concept. *Physical Review E* 1998; **58**:3955–3963.
37. Xi HW, Peng GW, Chou S-H. Finite-volume lattice Boltzmann method. *Physical Review E* 1999; **59**:6202–6205.
38. Ubertini S, Bella G, Succi S. Unstructured lattice Boltzmann equation with memory. *Mathematics and Computers in Simulation* 2006; **72**:237–241.

DOI: 10.1002/fld

39. Lee T, Lin C-L. A characteristic Galerkin method for discrete Boltzmann equation. *Journal of Computational Physics* 2001; **171**:336–356.
40. Jiang GS, Shu CW. Efficient implementation of weighted ENO schemes. *Journal of Computational Physics* 1996; **126**:202–228.
41. Guo ZL, Zheng CG, Shi BC. Non-equilibrium extrapolation method for velocity and boundary conditions in the lattice Boltzmann method. *Chinese Physics* 2002; **11**(4):366–374.

DOI: 10.1002/fld